Motion-selective coherent population trapping for subrecoil cooling of optically trapped atoms outside the Lamb-Dicke regime

Hyun Gyung Lee, Sooyoung Park, Meung Ho Seo, and D. Cho*
Department of Physics, Korea University, Seoul 02841, Republic of Korea

(Received 27 May 2022; accepted 8 August 2022; published 31 August 2022)

We propose a scheme that combines velocity-selective coherent population trapping (CPT) and Raman sideband cooling (RSC) for subrecoil cooling of optically trapped atoms outside the Lamb-Dicke regime. This scheme is based on an inverted Y configuration in an alkali-metal atom. It consists of a Λ formed by two Raman transitions between the ground hyperfine levels and the D transition, allowing RSC along two paths and formation of a CPT dark state. Using the state-dependent difference in vibration frequency of the atom in a circularly polarized trap, we can tune the Λ to make only the motional ground state a CPT dark state. We call this scheme motion-selective coherent population trapping (MSCPT). We write the master equations for RSC and MSCPT and solve them numerically for a ^{87}Rb atom in a one-dimensional optical lattice when the Lamb-Dicke parameter is 1. Although MSCPT reaches the steady state slowly compared with RSC, the former consistently produces colder atoms than the latter. The numerical results also show that subrecoil cooling by MSCPT outside the Lamb-Dicke regime is possible under a favorable, yet experimentally feasible, condition. We explain this performance quantitatively by calculating the relative darkness of each motional state. Finally, we discuss the application of the MSCPT scheme to an optically trapped diatomic polar molecule whose Stark shift and vibration frequency exhibit large variations depending on the rotational quantum number.

DOI: 10.1103/PhysRevA.106.023324

I. INTRODUCTION

Recoil by emission of final photons is the last hurdle in laser cooling atoms to a standstill. Besides evaporative cooling, which entirely avoids laser lights, two schemes have been developed to overcome the hurdle: Raman sideband cooling (RSC) [1] for trapped atoms and velocity-selective coherent population trapping (VSCPT) [2] for free atoms. Both methods achieve subrecoil cooling by using an arrangement that makes the motional ground state dark owing to either energy conservation or quantum interference, respectively. Although they are efficient tools, they are applicable in rather limited cases. Raman sideband cooling, which was originally developed for ions in a tight trap, can achieve subrecoil cooling only when the vibrational energy spacing $\hbar\nu$ of a trap is much larger than the recoil energy $\mathcal{E}_R$ or equivalently when the Lamb-Dicke parameter $\eta_{\rm LD}$, defined by $\eta_{\rm LD}^2 = \mathcal{E}_R/\hbar\nu$, is much less than 1. For optically trapped neutral atoms, the condition is not satisfied unless a lattice configuration with submicron confinement is employed [3,4] Subrecoil cooling by VSCPT has been demonstrated only for metastable He atoms with zero nuclear spin. Efforts to apply the scheme to alkali-metal atoms, such as gray molasses [5], have achieved only sub-Doppler cooling, and VSCPT is not applicable to trapped atoms.

In this paper we propose a cooling method that combines VSCPT and RSC so that they complement each other to overcome the limits they have when applied separately. Using the method, we aim to achieve subrecoil cooling of alkali-metal atoms in an optical trap even when the Lamb-Dicke condition is not satisfied. If we approach the aim starting from VSCPT, there are three main issues. (i) Owing to the hyperfine structure, any Λ configuration formed by a pair of D transitions of an alkali-metal atom has a leakage path out of it, complicating the arrangement for coherent population trapping (CPT) in a steady state. (ii) There is no velocity selection for bound-state atoms and we need a scheme that selects the motional ground state as a CPT dark state. (iii) By itself, VSCPT is only a diffusive process [6] and an extra cooling mechanism is needed, especially in two and three dimensions. (i) For the leakage problem, we have proposed an inverted Y configuration [7] consisting of a Λ formed by two ground hyperfine transitions from the states $|\phi_1\rangle$ and $|\phi_2\rangle$ to the apex state $|\phi_3\rangle$ that is coupled to the excited state $|\phi_4\rangle$ by the D transition (Fig. 1). Using ^{7}Li in an optical trap, we have demonstrated that the CPT phenomena of the inverted Y in a wide range of experimental parameters could be precisely described by a leak-free Λ system. (ii) For the motional selectivity, we use a circularly polarized trap beam. The vector polarizability β causes $|\phi_1\rangle$ and $|\phi_2\rangle$ to have different well depths and hence different vibration frequencies ν_1 and ν_2, respectively, as shown in Fig. 2. Thus, two-photon detuning between the motional states $|\phi_1, \chi_1(n)\rangle$ and $|\phi_2, \chi_2(n)\rangle$ depends on the vibrational quantum number n, and we can tune the Λ fields so that only the $n = 0$ pair forms a CPT dark state. We call this scheme motion-selective coherent population trapping (MSCPT). (iii) For the cooling, we propose to replace two radio-frequency (rf) fields used in our previous work [7] with two pairs of Raman beams, each of which is

*cho@korea.ac.kr

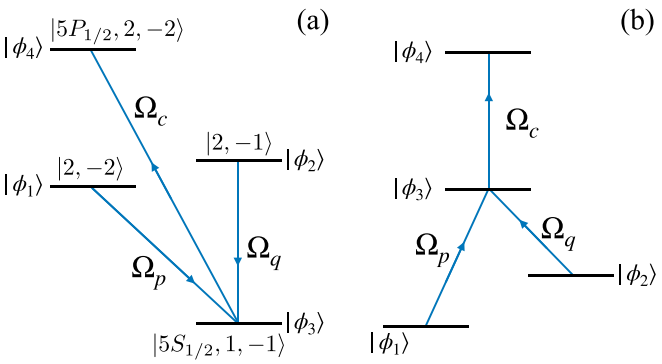

FIG. 1. (a) Raman transitions Ω_p and Ω_q and the D_1 transition Ω_c in ^{87}Rb for the cooling scheme of motion-selective coherent population trapping. (b) Inverted Y configuration for more intuitive visualization of the MSCPT scheme.

red detuned for the sideband cooling. From the viewpoint of RSC, by adding the $|\phi_2\rangle \rightarrow |\phi_3\rangle$ transition to a usual one of $|\phi_1\rangle \rightarrow |\phi_3\rangle$, we have a Λ configuration with the possibility of forming a CPT state. The difference between ν_1 and ν_2 allows us to select the pair of $n = 0$ states for CPT, providing them extra protection from the recoil heating. Another advantage is that there is no need for repumping atoms fallen to the $|\phi_2\rangle$ state, which reduces the average recoil heating for an optical pumping cycle in MSCPT.

There are two critical parameters for the success of the MSCPT cooling scheme: the difference $\Delta\nu_{12} = \nu_1 - \nu_2$ that introduces the motional selectivity and the coherence decay rate γ_{12} that destroys it. Because $\Delta\nu_{12}$ is proportional to β, heavy alkali-metal atoms with large spin-orbit coupling are favored. For a ^{87}Rb atom in an optical trap at a wavelength of 980 nm, $\Delta\nu_{12}$ is $2\pi \times 25$ Hz when $\eta_{\mathrm{LD}} = 1$, whereas the full width at half maximum (FWHM) of the CPT resonance

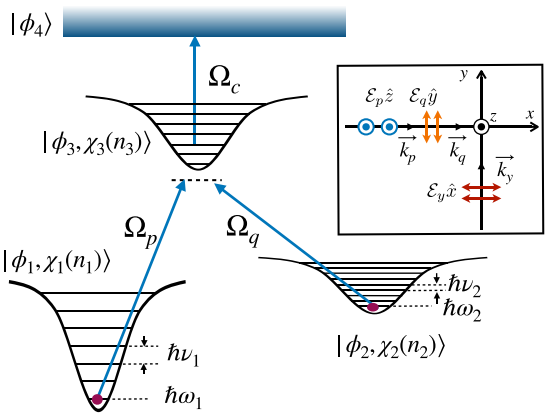

FIG. 2. Inverted Y configuration for an atom in an optical trap. The p and q transitions are red detuned for sideband cooling, and difference between the vibration frequencies ν_1 and ν_2 is responsible for motional selectivity. The difference is exaggerated. Here $\hbar\omega_1$ and $\hbar\omega_2$ are the ground-state energies of a trapped atom in the $|\phi_1\rangle$ and $|\phi_2\rangle$ states, respectively. The inset shows an arrangement of three laser beams $\vec{E}_p$, $\vec{E}_q$, and $\vec{E}_y$ for p and q transitions. Here the momentum transfers $\hbar\Delta\vec{k}_p$ and $\hbar\Delta\vec{k}_q$ to an atom by the two Raman transitions are the same.

in the inverted Y was 150 Hz in the rf experiment. Sources that contribute to γ_{12} are fluctuations in magnetic field and a phase noise between the pair of Raman beams. In Ref. [7] we reduced γ_{12} to 1.5 s^{-1}, which corresponds to a FWHM of 0.25 Hz in rf spectroscopy, by shielding the ambient field and controlling the current noise. The γ_{12} originating from the Raman phase noise can be easily reduce below 1 s^{-1} using modulation and phase-locking techniques. Nevertheless, this implies that cooling by MSCPT requires precautions normally reserved for precision spectroscopy. When the atomic density is high, collisions can dephase a CPT state [8], and the D beam, which couples $|\phi_3\rangle$ to $|\phi_4\rangle$, may mediate photoassociation and subsequent heating and loss of the atoms. In this regard, MSCPT is best suited for cooling single atoms in an optical lattice or a tweezer. In addition, cooling by MSCPT is slower than that by RSC because even a pair with nonzero n can form a partially dark superposition state, hampering the sideband cooling. Some high-n states may also form parasitic CPT dark states.

In spite of these difficulties, we recently demonstrated the effectiveness of the MSCPT scheme in an experiment using ^{87}Rb atoms in a one-dimensional (1D) optical lattice [9]. We observed CPT phenomena driven by a pair of stimulated Raman transitions and, by employing the MSCPT scheme, achieved lower temperature than that obtained by RSC. Finally, we envision using MSCPT to cool optically trapped polar molecules [10], whose Stark shift exhibits a strong dependence on the rotational quantum number. However, for this application, finding an appropriate configuration for robust CPT is a prerequisite.

In the following sections we describe the MSCPT scheme in more detail and present the master equations and the results of the numerical simulations. Using RSC as a benchmark, we evaluate the performance of MSCPT in terms of the steady-state distribution of atoms over n and the dynamics toward it.

II. MOTION-SELECTIVE COHERENT POPULATION TRAPPING

The backbone of the MSCPT scheme is the arrowlike configuration shown in Fig. 1(a), where we use ^{87}Rb as an example. In Fig. 1(b) it is transformed to an inverted Y configuration for more intuitive visualization. It consists of a Λ formed by the ground hyperfine transitions $|\phi_1\rangle = |5S_{1/2}, F = 2, m_F = -2\rangle \rightarrow |\phi_3\rangle = |F = 1, m_F = -1\rangle$ and $|\phi_2\rangle = |F = 2, m_F = -1\rangle \rightarrow |\phi_3\rangle$, which we will call p and q transitions, respectively, and the D_1 coupling from the apex state $|\phi_3\rangle$ to the excited state, $|\phi_4\rangle = |5P_{1/2}, F = 2, m_F = -2\rangle$. Here F is the total angular momentum and m_F is its z component. The D_1 coupling opens a path for $|\phi_3\rangle$ to decay to a CPT dark state via $|\phi_4\rangle$. Angular momentum conservation dictates that $|\phi_4\rangle$ decays only to one of the three states in the Λ, and the inverted Y is closed. The D_1 is favored over the D_2 coupling owing to the simple hyperfine structure of the $5P_{1/2}$ state. An equivalent inverted Y configuration can be identified in all alkali-metal atoms. The master equations for the inverted Y [11] can be reduced to those for an effective Λ system by adiabatically eliminating $|\phi_4\rangle$ owing to its short lifetime [7]. Unlike a typical Λ formed by two D couplings, this effective Λ allows us to choose the decay rate R of the $|\phi_3\rangle$ state by

adjusting the D_1 coupling strength as

$$R = \frac{1}{2}\frac{|\Omega_c|^2/2}{\Delta_c^2 + \Gamma^2/4}\Gamma, \tag{1}$$

where Γ is the decay rate of $|\phi_4\rangle$ and Ω_c and Δ_c are the Rabi frequency and the detuning of the D_1 coupling, respectively.

Considering a ^{87}Rb atom in an optical trap of a circularly polarized Gaussian beam with peak intensity I_0, the trap depth for the $|5S_{1/2}, F, m_F\rangle$ state is [12]

$$U_0(F, m_F) = (\alpha + \beta g_F m_F) 2\mu_0 c I_0, \tag{2}$$

where α and β are the scalar and vector polarizabilities, respectively, and g_F is the Landé g factor. The fractional change in the vibration frequency of the $|F, m_F\rangle$ state with respect to ν_0 of the $m_F = 0$ state is $(\beta/2\alpha) g_F m_F$. If the Raman fields, denoted by Ω_p and Ω_q in Fig. 2, are tuned to the Λ transition between the pair of motional ground states, the $|\phi_1, \chi_1(n)\rangle$ and $|\phi_2, \chi_2(n)\rangle$ states have a two-photon detuning $n\Delta\nu_{12}$, making their CPT-like superposition state progressively brighter as n increases. Here

$$\Delta\nu_{12} = \frac{\beta}{4\alpha}\nu_0 \tag{3}$$

for the configuration in Fig. 1(a).

In MSCPT, each of the $|\phi_1, \chi_1(n_1)\rangle$ and $|\phi_2, \chi_2(n_2)\rangle$ states can make stimulated Raman transitions to $|\phi_3, \chi_3(n_3)\rangle$ for a range of n_3. The Rabi frequency for the p transition $|\phi_1, \chi_1(n_1)\rangle \to |\phi_3, \chi_3(n_3)\rangle$ is

$$\Omega_p(n_3, n_1) = \Omega_p^0 \mathcal{F}_{31}(n_3, n_1), \tag{4}$$

where Ω_p^0 is the Rabi frequency for a free atom and the Franck-Condon factor is defined by

$$\mathcal{F}_{31}(n_3, n_1) = \langle \chi_3(n_3)| e^{i\Delta\vec{k}_p\cdot\vec{r}} |\chi_1(n_1)\rangle. \tag{5}$$

Here $\hbar\Delta\vec{k}_p$ is the linear momentum transfer by the pair of Raman beams for the p transition and $\vec{r}$ is the center-of-mass coordinate of the atom. Similarly, for the q transition $|\phi_2, \chi_2(n_2)\rangle \to |\phi_3, \chi_3(n_3)\rangle$, $\Omega_q(n_3, n_2) = \Omega_q^0 \mathcal{F}_{32}(n_3, n_2)$, where $\hbar\Delta\vec{k}_q$ is the momentum transfer. For the pair $\{|\phi_1, \chi_1(n)\rangle, |\phi_2, \chi_2(n)\rangle\}$ to form a CPT dark state, the transition amplitudes for all allowed p and q transitions to the two respective groups of $|\phi_3, \chi_3(n_3)\rangle$ should interfere destructively. This is possible if $\Delta\vec{k}_p = \Delta\vec{k}_q$ so that $\mathcal{F}_{31}(n_3, n) = \mathcal{F}_{32}(n_3, n)$ and the pair of states share the target group. The inset in Fig. 2 shows one arrangement of laser beams for the Raman transitions in Fig. 1(a) that satisfy $\Delta\vec{k}_p = \Delta\vec{k}_q$. Specifically, the p transition is driven by $\vec{E}_y = \mathcal{E}_y\hat{x}\cos(k_y y - \omega_y t)$ and $\vec{E}_p = \mathcal{E}_p\hat{z}\cos(k_p x - \omega_p t)$ with $\Delta\vec{k}_p = \vec{k}_p - \vec{k}_y$ and the q transition by $\vec{E}_y$ and $\vec{E}_q = \mathcal{E}_q\hat{y}\cos(k_q x - \omega_q t)$ with $\Delta\vec{k}_q = \vec{k}_q - \vec{k}_y$. Here $\Delta\vec{k}_p = \Delta\vec{k}_q$ to a very good approximation with a discrepancy originating from the Zeeman shift of less than 1 MHz between $|\phi_1\rangle$ and $|\phi_2\rangle$. Because $|\chi_1(n)\rangle$ and $|\chi_2(n)\rangle$ are different, $\mathcal{F}_{31}(n_3, n)$ and $\mathcal{F}_{32}(n_3, n)$ are not identical, and this may complicate the CPT formation as well. However, this discrepancy affects, to first order, only the amplitudes of $|\phi_1, \chi_1(n)\rangle$ and $|\phi_2, \chi_2(n)\rangle$ in a dark superposition state, and the simulations show that the effects are insignificant for the experimentally feasible range of $\Delta\nu_{12}/\nu_0$.

III. MASTER EQUATIONS

Although the 2D configuration in the inset of Fig. 2 is a natural realization of the MSCPT scheme, we limit our discussion to the master equations and their numerical solutions in one dimension. Extending the formalism to two dimensions is burdensome but straightforward. However, with our computing resources, numerical simulations are feasible only in one dimension when states with a sufficiently large n are included. We also focus on single atoms and ignore collisions between them.

A. Raman sideband cooling in one dimension

For 1D RSC, we consider a system consisting of only the states $|\phi_1, \chi_1(n_1)\rangle$, $|\phi_3, \chi_3(n_3)\rangle$, and $|\phi_4\rangle$ in Fig. 2. The Hamiltonian for this system is

$$H_{\rm RSC} = H_0 + W_p + V, \tag{6}$$

where H_0 is for a trapped atom, W_p for the p transition, and V for dissipative processes. Although the difference between ν_1 and ν_3 is irrelevant in RSC, we distinguish $|\chi_1\rangle$ and $|\chi_3\rangle$ to ensure a formalism consistent with that of MSCPT. The master equation for the density matrix ρ is

$$i\hbar\frac{d\rho}{dt} = [H_0 + W_p, \rho] + \left(\frac{\partial\rho}{\partial t}\right), \tag{7}$$

where the second term represents the dissipative processes. Explicitly,

$$H_0 = \sum_{j=1,3}\sum_{n_j''}(\hbar\omega_j + \hbar\nu_j n_j'')|\phi_j, \chi_j(n_j'')\rangle\langle\phi_j, \chi_j(n_j'')|, \tag{8a}$$

$$W_p = \frac{\hbar\Omega_p^0}{2}e^{-i\omega_p' t}\sum_{n_1'', n_3''}\mathcal{F}_{31}(n_3'', n_1'')|\phi_3, \chi_3(n_3'')\rangle\langle\phi_1, \chi_1(n_1'')| + \text{H.c.}, \tag{8b}$$

where $\hbar\omega_j$ is the energy of the lowest vibrational state $|\phi_j, \chi_j(0)\rangle$ and $\omega_p' = \omega_y - \omega_p$. In the 1D formalism, $\Delta\vec{k}_p = k_p\hat{x}$ is substituted in Eq. (5); $\mathcal{F}_{31}(n_3, n_1) = \langle\chi_3(n_3)|e^{ik_p x}|\chi_1(n_1)\rangle$. The master equations, which include the decay of the $|\phi_3\rangle$ state at the rate R in Eq. (1), can be expressed in terms of $\eta_{jj}(n_j, n_j') = \rho_{jj}(n_j, n_j')$ for $j = 1, 3$ and $\eta_{13}(n_1, n_3) = \rho_{13}(n_1, n_3)e^{-i\omega_p' t}$ as

$$\begin{aligned}\dot{\eta}_{11}(n_1, n_1') = i\frac{\Omega_p^0}{2}\sum_{n_3''}\{&\eta_{13}(n_1, n_3'')\mathcal{F}_{31}(n_3'', n_1') \\ &- \mathcal{F}_{13}^*(n_1, n_3'')\eta_{31}(n_3'', n_1')\} \\ &+ i(n_1' - n_1)\nu_1\eta_{11}(n_1, n_1') + \delta_{n_1, n_1'}p_1 R \\ &\times\sum_{n_3''}|\mathcal{F}_{13}(n_1, n_3'')|^2\eta_{33}(n_3'', n_3''),\end{aligned} \tag{9a}$$

$$\begin{aligned}\dot{\eta}_{33}(n_3, n_3') = i\frac{\Omega_p^0}{2}\sum_{n_1''}\{&\eta_{31}(n_3, n_1'')\mathcal{F}_{13}^*(n_1'', n_3') \\ &- \mathcal{F}_{31}(n_3, n_1'')\eta_{13}(n_1'', n_3')\}\end{aligned}$$

$$+\{i(n_3'-n_3)\nu_3-R\}\eta_{33}(n_3,n_3')+\delta_{n_3,n_3'}p_3R \times\sum_{n_3''}|\mathcal{F}_{33}(n_3,n_3'')|^2\eta_{33}(n_3'',n_3''), \tag{9b}$$

$$\dot\eta_{13}(n_1,n_3)=i\frac{\Omega_p^0}{2}\Bigg\{\sum_{n_1''}\eta_{11}(n_1,n_1'')\mathcal{F}_{13}^*(n_1'',n_3) -\sum_{n_3''}\mathcal{F}_{13}^*(n_1,n_3'')\eta_{33}(n_3'',n_3)\Bigg\} +\Big(i[(n_3+\Delta n)\nu_3-n_1\nu_1]-\frac{R}{2}\Big) \times\eta_{13}(n_1,n_3), \tag{9c}$$

and $\dot\eta_{31}(n_3,n_1)=\dot\eta_{13}^*(n_1,n_3)$. We use the rotating-wave approximation. Here Δn, which is defined as $\omega_p'-(\omega_3-\omega_1)=-\Delta n\nu_3$, represents the order of the red sideband. The last terms in Eqs. (9a) and (9b) describe the decay of $|\phi_3,\chi_3(n_3'')\rangle$ to $|\phi_1,\chi_1(n_1)\rangle$ and $|\phi_3,\chi_3(n_3)\rangle$ with branching ratios p_1 and p_3, respectively, as a process of emitting a photon with a momentum $\hbar k_p$. The $\mathcal{F}$ factors satisfy the relation [13]

$$\sum_{n_i''=0}^{\infty}E_i(n_i'')|\mathcal{F}_{ij}(n_i'',n_j)|^2-E_j(n_j)=\mathcal{E}_R, \tag{10}$$

and the recoil heating by $\mathcal{E}_R=\hbar^2k_p^2/2m$, where m is the atomic mass, accompanying the decay is built into the master equations. Here $E_j(n_j)=\hbar\nu_j(n_j+\frac{1}{2})$, $j=1,3$, is the motional energy of the $|\chi_j(n_j)\rangle$ state. However, the real process is an excitation to $|\phi_4\rangle$ by an absorption and a subsequent decay by a spontaneous emission. When averaged over the angular distribution of the emission, the total heating is $2\mathcal{E}_R$. In numerical simulations, we take this into account by using the branching ratios $p_1'=p_1/2$ and $p_3'=1-p_1/2$ to double the number of emissions required to optically pump an atom from $|\phi_3\rangle$ to $|\phi_1\rangle$.

In an experiment, parametric heating from trap noise and depumping of the $|\phi_1\rangle$ state by an imperfect optical pumping are common problems. The transition rate from the motional state $|\chi(n)\rangle$ to $|\chi(n\pm2)\rangle$ driven by the intensity noise of a trap beam is approximated as

$$Q_\pm(n)=\frac{\pi\nu^2}{16}S(2\nu)(n+1\pm1)(n\pm1), \tag{11}$$

where $S(2\nu)$ is the power spectral density of the fractional intensity noise at twice the vibration frequency [14]. Its effect on the master equations can be included by adding $\dot\eta_{jj}^{\mathrm{Q}}(n,n)$ and $\dot\eta_{ij}^{\mathrm{Q}}(n_i,n_j)$ to $\dot\eta_{jj}(n,n)$ and $\dot\eta_{ij}(n_i,n_j)$, respectively,

$$\dot\eta_{jj}^{\mathrm{Q}}(n,n)=-Q(n)P_j(n)+Q_+(n-2)P_j(n-2)+Q_-(n+2)P_j(n+2), \tag{12a}$$

$$\dot\eta_{ij}^{\mathrm{Q}}(n_i,n_j)=-\tfrac{1}{2}\{Q(n_i)+Q(n_j)\}\eta_{ij}(n_i,n_j), \tag{12b}$$

where $P_j(n)=\eta_{jj}(n,n)$ and $Q(n)=Q_+(n)+Q_-(n)$. Similarly, the effect of an unintended transition of the $|\phi_1\rangle$ state to an excited state $|\phi_e\rangle$ can be included by adding $\dot\eta_{jj}^{\mathrm{D}}(n,n)$ and $\dot\eta_{ij}^{\mathrm{D}}(n_i,n_j)$ to $\dot\eta_{jj}(n,n)$ and $\dot\eta_{ij}(n_i,n_j)$, respectively,

$$\dot\eta_{jj}^{\mathrm{D}}(n,n)=-DP_j(n)\delta_{j1}+p_jD\sum_{n_1''}|\mathcal{F}_{j1}(n_j,n_1'')|^2P_1(n_1''), \tag{13a}$$

$$\dot\eta_{ij}^{\mathrm{D}}(n_i,n_j)=-\tfrac{1}{2}D(\delta_{i1}+\delta_{j1})\eta_{ij}(n_i,n_j), \tag{13b}$$

where D is the effective decay rate of the $|\phi_1\rangle$ state, and we assume that $|\phi_e\rangle$ has the same branching ratios p_1 and p_3 as $|\phi_4\rangle$.

B. Motion-selective coherent population trapping in one dimension

For 1D MSCPT in Fig. 2, $H_{\mathrm{MSCPT}}=H_{\mathrm{RSC}}+W_q$ and H_0 for a trapped atom in Eq. (8a) is augmented by

$$\sum_{n_2''=0}^{\infty}(\hbar\omega_2+\hbar\nu_2n_2'')|\phi_2,\chi_2(n_2'')\rangle\langle\phi_2,\chi_2(n_2'')|. \tag{14}$$

For the q transition W_q is

$$W_q=\frac{\hbar\Omega_q^0}{2}e^{-i\omega_q't}\sum_{n_2'',n_3''}\mathcal{F}_{32}(n_3'',n_2'')|\phi_3,\chi_3(n_3'')\rangle\langle\phi_2,\chi_2(n_2'')| +\mathrm{H.c.}, \tag{15}$$

where $\omega_q'=\omega_y-\omega_q$. The angular momentum selection rule and the condition $|\omega_1-\omega_2|\gg R$ forbid the p Raman fields from driving the q transition and vice versa. The master equations for 1D MSCPT are listed in Appendix A. Below we write the equation for $\dot\eta_{12}(n_1,n_2)$ only because it includes the critical terms that describe the motional selectivity and the decay of the CPT coherence:

$$\dot\eta_{12}(n_1,n_2)=\frac{i}{2}\sum_{n_3''}\{\Omega_q^0\eta_{13}(n_1,n_3'')\mathcal{F}_{32}(n_3'',n_2) -\Omega_p^0\mathcal{F}_{13}^*(n_1,n_3'')\eta_{32}(n_3'',n_2)\} +\{i(n_2\nu_2-n_1\nu_1-\delta_{\mathrm{CPT}})-\gamma_{12}\}\eta_{12}(n_1,n_2). \tag{16}$$

Here $\delta_{\mathrm{CPT}}=(\omega_p'-\omega_q')-(\omega_2-\omega_1)$ is the detuning of the p and q Raman fields from the CPT resonance of the motional ground states and γ_{12} is the coherence decay rate. The effects of parametric heating and depumping can be incorporated as done in RSC.

IV. NUMERICAL SIMULATIONS

Given experimental parameters for either RSC or MSCPT, we are interested in the distribution $P(n)=\sum_j\eta_{jj}(n,n)$ of atoms in a steady state and the dynamics toward it. By reshaping $\eta_{ij}(n_i,n_j)$ into an N-dimensional column vector x, the master equations can be written as $\dot x=Ax$ with an appropriately defined matrix A. If the maximum n to be included in a calculation is n_c, $N=4(n_c+1)^2$ for 1D RSC and $9(n_c+1)^2$ for 1D MSCPT. A steady-state solution x_s satisfies $Ax_s=0$ under the constraint $\sum_nP(n)=1$. We use the Moore-Penrose algorithm for pseudoinversion to solve the equation. When

$n_c = 100$, the runtime on a personal computer [15] to obtain x_s is 3 min for RSC and 30 min for MSCPT. Time evolution of x follows $x(t) = e^{At}x(0)$. We calculate $U(\tau) = e^{A\tau}$ for a time interval τ and obtain snapshots of $x(t)$ at $t = \tau, 2\tau, \ldots$ by repeatedly applying $U(\tau)$. We use τ near $\tau_1/10$, where τ_1 is the shorter time constant of a double-exponential decay of temperature to be discussed later. The calculation of $U(\tau)$ is demanding in terms of time and memory, and the runtime for RSC with $n_c = 75$ is 1 h. For MSCPT, we limit n_c to 65 and use single precision to calculate $U(\tau)$ in 2 h. For the numerical solutions, we need the values of the Franck-Condon factors $\mathcal{F}_{ij}(n_i, n_j)$. When $\eta_{\rm LD} \geqslant 1$, for a given n_j, the range of n_i to be calculated is large, and the evaluation of each $\mathcal{F}_{ij}(n_i, n_j)$ is time consuming because the polynomial expansion of $e^{ik_p x}$ does not converge. To efficiently calculate the $\mathcal{F}$ factors, we develop recursion relations. The relations are summarized in Appendix B. The calculated results are validated by the sum rule $\sum_{n_i''=0}^{\infty} |\mathcal{F}_{ij}(n_i'', n_j)|^2 = 1$, based on the completeness of $|\chi_i(n_i)\rangle$ and the unitarity of $e^{ik_p x}$. In Appendix B we also include the case of $k_p = 0$ for a transition by a rf field.

As a model system, we use a 1D optical lattice in our apparatus [16]. Its wavelength $\lambda_{\rm OL}$ is 980 nm, at which $\alpha = -873$ and $\beta = -25$ in atomic units for ^{87}Rb. We adjust the minimum spot size w_0 to 10 μm and the well depth in units of the Boltzmann constant k_B to 125 μK so that $\nu_0 = 2\pi \times 3.5$ kHz and $\eta_{\rm LD} \simeq 1$ for the transverse motion. When the lattice beam is circularly polarized, $\Delta\nu_{12}$ is $2\pi \times 25$ Hz. For a ^{87}Rb atom in Fig. 1(a), the branching ratios from $|\phi_4\rangle$ to $|\phi_1\rangle$, $|\phi_2\rangle$, and $|\phi_3\rangle$ are $p_1 = \frac{1}{3}$, $p_2 = \frac{1}{6}$, and $p_3 = \frac{1}{2}$, respectively. On average, three optical pumping cycles are needed to put an atom into $|\phi_1\rangle$ in RSC and two cycles to put it into either $|\phi_1\rangle$ or $|\phi_2\rangle$ in MSCPT. However, we use $p_1 = \frac{1}{2}$ for RSC and $p_1 = p_2 = \frac{1}{4}$ for MSCPT in the following simulations to compare the cooling efficiencies while the recoil heating rates are the same. In addition, as discussed previously, we use $p_1' = \frac{1}{4}$ for RSC and $p_1' = p_2' = \frac{1}{8}$ for MSCPT to take into account additional heating from the absorption of an optical pumping photon. We use R, Ω_p, and Ω_q equal to ν_0, and $\gamma_{12} = 3 \times 10^{-4}\nu_0$ or $2\pi \times 1$ Hz as benchmark values. The two pairs of Raman beams are tuned to $\delta_{\rm CPT} = 0$ so that the $n = 0$ states are CPT resonant.

First, we calculate $P(n)$ versus the order Δn of the red sideband for both RSC and MSCPT. Figure 3(a) shows $P5 = \sum_{n=0}^{5} P(n)$ versus Δn and Fig. 3(b) shows $T5 = -6\hbar\nu_0/k_B \ln(1 - P5)$ in units of $T_R = \mathcal{E}_R/k_B$. Here $T_R = 175$ nK and $T5$ is the temperature that produces $P5$ under the Maxwell-Boltzmann (MB) distribution. $T5$ is a better measure of temperature than one by fitting $P(n)$ to the MB distribution because without atomic collisions, $P(n)$ reflects the details of the $\mathcal{F}$ factors and does not follow the MB distribution. We choose $P5$ because $dP5/dT$ is maximum at around $T = 3T_R$, the temperature range of interest in Fig. 3(b). The minimum Δn to overcome the recoil heating in either RSC or MSCPT is 4 when $\eta_{\rm LD} = 1$. For RSC, $\Delta n = 6$ produces the lowest $T5$ owing to the radiative broadening of the Raman transition by R. Reducing R results in the optimal order $\Delta n_{\rm opt}$ approaching 4 and a lower temperature; however, this is at the expense of slower cooling. Although the simulation produces smooth reduction of $P5$ to finite values when $\Delta n \leqslant 3$, it is

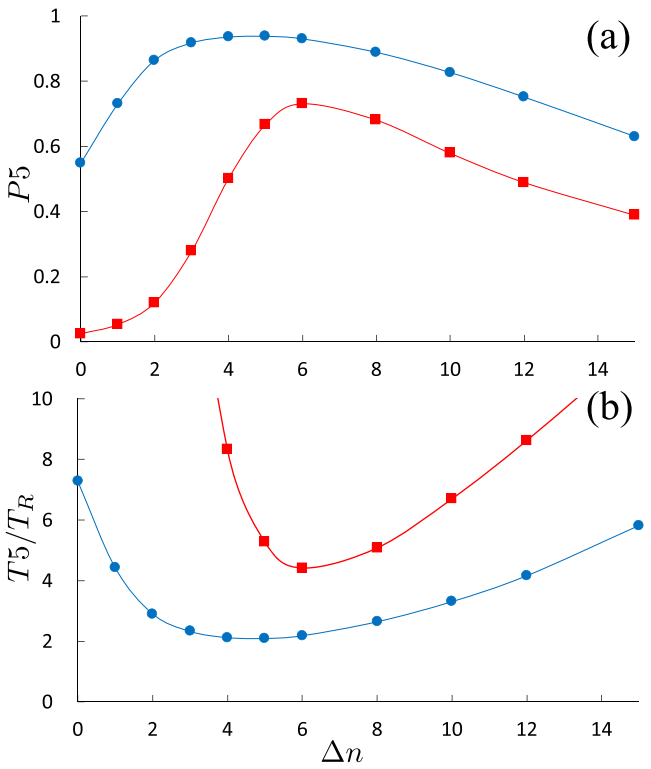

FIG. 3. (a) Plot of $P5$, the sum of the steady-state population with the motional quantum number n below 5, versus the order Δn of the red sideband. We use the benchmark condition described in the text. Red squares are for RSC and blue circles are for MSCPT. (b) Plot of $T5$, the temperature calculated from $P5$ assuming the Maxwell-Boltzmann distribution, in units of $T_R = \mathcal{E}_R/k_B$ versus Δn. Here $\mathcal{E}_R$ is the recoil energy accompanying emission of a photon and k_B is the Boltzmann constant. The lowest $T5$ produced by MSCPT is $2T_R$, while that by RSC is $4.5T_R$.

an artifact of truncating n at n_c. In an experiment, atoms are expected to boil out in this condition. For MSCPT, $\Delta n_{\rm opt} = 5$ and $P5$ shows a gradual decrease away from it. Motion-selective CPT consistently produces a lower temperature than RSC, with the lowest $T5$ of $2T_R$ compared with $4.5T_R$ by RSC. If the real value of $p_1 = \frac{1}{3}$ for RSC is used, $\Delta n_{\rm opt}$ is 7, and the minimum $T5$ is $6T_R$, three times higher than that by MSCPT.

The better performance of MSCPT is a consequence of the CPT-induced darkness of the low-n states. We define the brightness of the nth pair of states $\{|\phi_1, \chi_1(n)\rangle, |\phi_2, \chi_2(n)\rangle\}$ in MSCPT as a product of R and the population in the $|\phi_3\rangle$ state,

$$\mathcal{B}(n) = R \sum_{n_3=0}^{n_c} P_3(n_3). \tag{17}$$

The $\mathcal{B}(n)$ of the nth state $|\phi_1, \chi_1(n)\rangle$ in RSC can be similarly defined. We obtain $\mathcal{B}(n)$ for MSCPT or RSC by solving the master equations in a reduced Hilbert space consisting of the nth pair or the nth state, respectively, and $\{|\phi_3, \chi_3(n_3)\rangle, n_3 = 0, 1, \ldots, n_c\}$. Figure 4(a) shows $\mathcal{B}(n)/R$ at the respective $\Delta n_{\rm opt}$ of RSC and MSCPT. The low-n states in MSCPT are significantly darker than those in RSC. We expect $P(n)$ to be inversely proportional to $\mathcal{B}(n)$. In Fig. 4(b), the red and blue curves of $P(0)[\mathcal{B}(0)/\mathcal{B}(n)]^a$ with $a = 1.7$ and 1.35 show

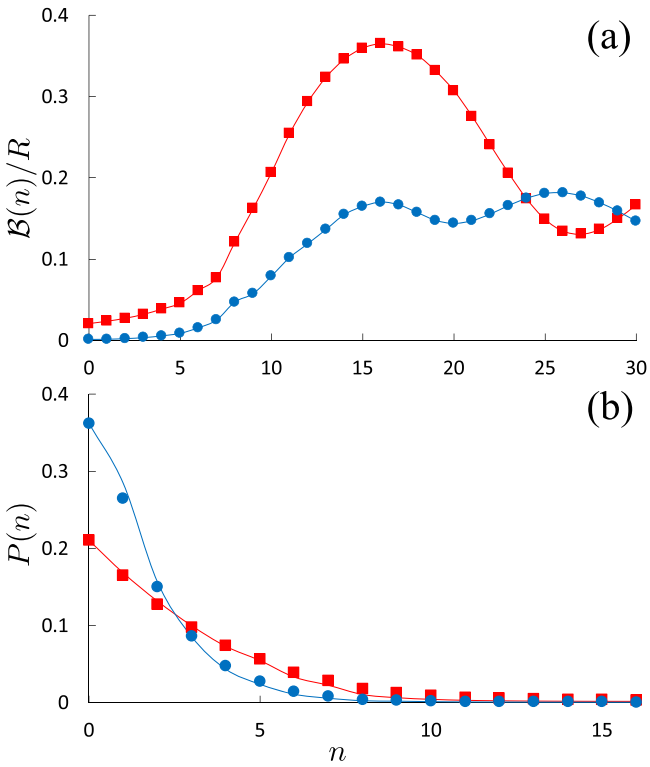

FIG. 4. Comparison of RSC and MSCPT in terms of the brightness $\mathcal{B}(n)$ of the nth state. Here $\mathcal{B}(n)$ is defined as the product of the effective decay rate R of the $|\phi_3\rangle$ state and the total population in the $|\phi_3\rangle$ state. (a) Brightness $\mathcal{B}(n)$ for RSC (red squares) and MSCPT (blue circles) in units of R. The low-n states in MSCPT are much darker than those in RSC. (b) Steady-state population $P(n)$ versus n. Here $P(n)$ is inversely proportional to $\mathcal{B}(n)$. The $P(n)$ is fitted by the red curve $P(0)[\mathcal{B}(0)/\mathcal{B}(n)]^{1.7}$ for RSC and by the blue curve $P(0)[\mathcal{B}(0)/\mathcal{B}(n)]^{1.35}$ for MSCPT.

good agreement with $P(n)$ of RSC and MSCPT, respectively. One drawback of this darkness is the slowdown of the cooling process. Figure 5 shows the evolution of $T5$ under the optimal RSC and MSCPT starting from the MB distribution at 3 μK. Both curves follow a double-exponential decay expressed as

$$T5(t) = (T_i - T_m)e^{-t/\tau_1} + (T_m - T_f)e^{-t/\tau_2} + T_f \qquad (18)$$

because, unlike a simple decay of the same entities, a qualitative change occurs in the atomic ensemble as the cooling proceeds. Here T_i, T_m, and T_f are the initial, middle, and final temperatures, respectively, and τ_1 and τ_2 are time constants. Although MSCPT produces a lower T_f, it is 5 times slower than RSC; specifically, $\tau_1 = 1.1$ ms and $\tau_2 = 7.7$ ms for RSC and $\tau_1 = 5.2$ ms and $\tau_2 = 34$ ms for MSCPT.

Next we change $\delta_{\rm CPT}$ of MSCPT while keeping $\Delta n = 5$. Figure 6(a) shows $T5/T_R$ versus $\delta_{\rm CPT}$ in units of $\Delta\nu_{12}$. The dashed horizontal line denotes $T5/T_R$ for RSC. According to Eq. (16) for $\dot{\eta}_{12}(n_1, n_2)$, the nth pair of states $\{|\phi_1, \chi_1(n)\rangle, |\phi_2, \chi_2(n)\rangle\}$ is CPT resonant when $\delta_{\rm CPT} = -n\Delta\nu_{12}$. As $\delta_{\rm CPT}$ becomes negative, $T5$ increases sharply as the $n = 1, 2, \ldots$ pairs successively become dark. The minimum $T5$ of RSC, $4.5T_R$, corresponds to the average n of 4, to which $T5$ of MSCPT becomes comparable when $\delta_{\rm CPT} =$

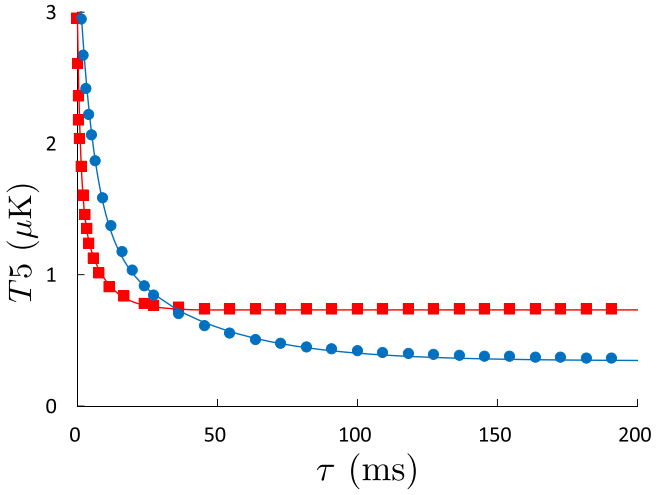

FIG. 5. Evolution of $T5$ for RSC (red squares) and MSCPT (blue circles) starting from the MB distribution at 3 μK. They are fitted by double-exponential decay curves with $\tau_1 = 1.1$ ms and $\tau_2 = 7.7$ ms for RSC (red solid line) and $\tau_1 = 5.2$ ms and $\tau_2 = 34$ ms for MSCPT (blue solid line).

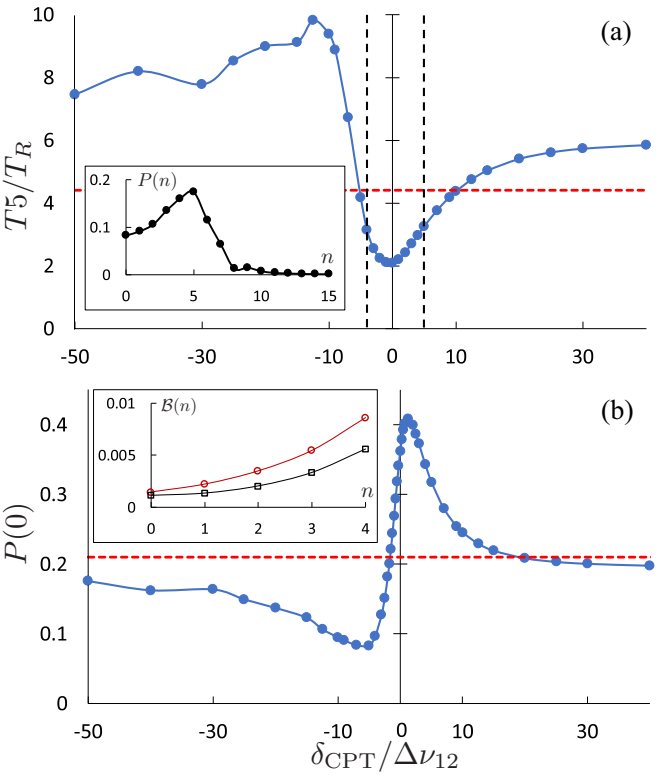

FIG. 6. (a) Plot of $T5$ in units of T_R versus $\delta_{\rm CPT}$ in units of $\Delta\nu_{12}$. Here $\delta_{\rm CPT}$ is the detuning of the p and q Raman fields from the CPT resonance of the motional ground states. The red dashed horizontal line represents $T5/T_R$ for RSC. The inset shows $P(n)$ when $\delta_{\rm CPT} = -5\Delta\nu_{12}$. (b) Ground-state population $P(0)$ versus $\delta_{\rm CPT}/\Delta\nu_{12}$. The inset shows that $\mathcal{B}(n)$ when $\delta_{\rm CPT} = 1.3\Delta\nu_{12}$ (red circles) increases more rapidly than $\mathcal{B}(n)$ when $\delta_{\rm CPT} = 0$ (black squares). This explains the shift of $P(0)$ maximum to $\delta_{\rm CPT} = 1.3\Delta\nu_{12}$.

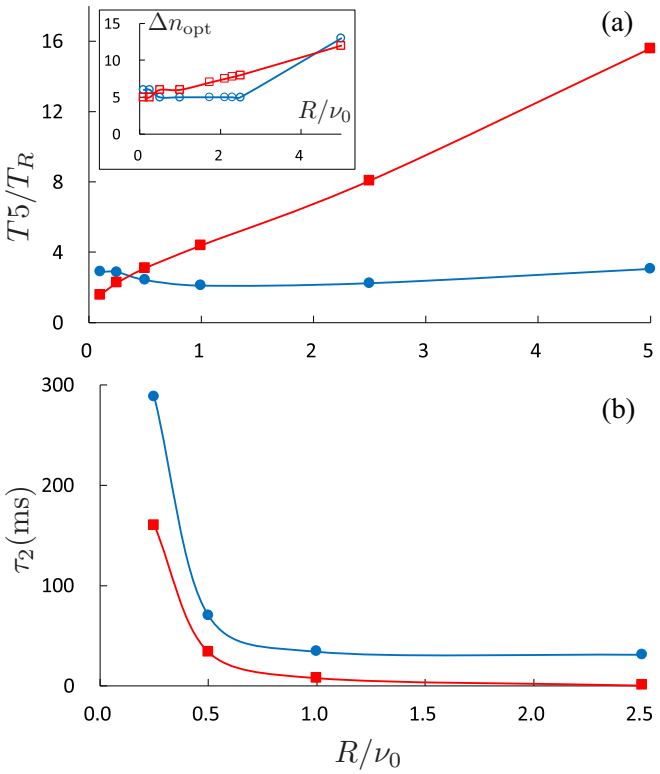

FIG. 7. (a) Plot of $T5/T_R$ of RSC (red squares) and MSCPT (blue circles) versus $R = \Omega_p = \Omega_q$ in units of ν_0. Each $T5$ is obtained at an optimal Δn for a given R. The dependence of the optimal Δn on R is shown in the inset. (b) Time constant τ_2 of RSC and MSCPT versus $R = \Omega_p = \Omega_q$.

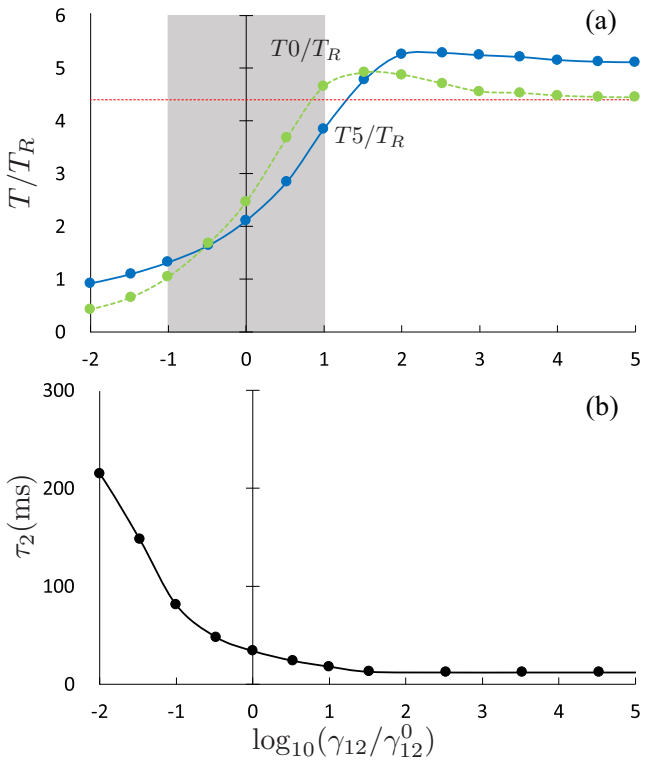

FIG. 8. (a) Plot of $T5/T_R$ (blue solid curve with circles) and $T0/T_R$ (green dashed curve with circles) of MSCPT versus $\log_{10}(\gamma_{12}/\gamma_{12}^0)$. $\gamma_{12}^0 = 2\pi \times 1$ Hz; $T0$ is defined from the ground-state population $P(0)$. The red dashed line represents $T5/T_R$ of RSC. The shaded area is where MSCPT is both effective and experimentally feasible. (b) Time constant τ_2 of $T5$ versus $\log_{10}(\gamma_{12}/\gamma_{12}^0)$. Although the temperature is lower at small γ_{12}, the cooling process becomes slower.

$-5\Delta\nu_{12}$. The inset of Fig. 6(a) shows $P(n)$ peaks at $n = 5$ when $\delta_{\rm CPT} = -5\Delta\nu_{12}$. For a positive $\delta_{\rm CPT}$, although detuning from the CPT resonance increases for all n pairs, that of the $n = 0$ pair is still the smallest. This explains the gradual increase in $T5$ for $\delta_{\rm CPT} > 0$. Figure 6(b) shows $P(0)$ versus $\delta_{\rm CPT}/\Delta\nu_{12}$. The $P(0)$ is maximum not at $\delta_{\rm CPT} = 0$ but at $1.3\Delta\nu_{12}$ because $d\mathcal{B}(n)/dn$ or the contrast is more critical than $\mathcal{B}(n)$ itself for determining $P(n)$, and the detuning puts $\mathcal{B}(n)$ on a slope near $n = 0$. The inset shows $\mathcal{B}(n)$ for $\delta_{\rm CPT} = 0$ (black squares) and $1.3\Delta\nu_{12}$ (red circles). The width between the vertical dashed lines in Fig. 6(a), where MSCPT shows a noticeable advantage, is $10\Delta\nu_{12}$ or 250 Hz. While the Raman fields can be easily tuned to within 1 Hz or better, $d\delta_{\rm CPT}/dB =$ 350 Hz/mG, where B is the quantization field strength, and precise control of the B field is a more demanding task in practice.

The effects of R, Ω_p, and Ω_q on the steady-state solution and the time constants are similar, and we set $R = \Omega_p = \Omega_q$, considering them as a single parameter. In Fig. 7(a) we plot $T5/T_R$ of RSC and MSCPT versus R. Each $T5$ is obtained at $\Delta n_{\rm opt}$ for a given R, and the dependence of $\Delta n_{\rm opt}$ on R for RSC (red squares) and MSCPT (blue circles) is shown in the inset. As R becomes large, the Raman transition broadens to increase $\mathcal{B}(n)$ of the low-n states, and $T5$ of RSC increases at $dT5/dR = 0.5\ \mu{\rm K}/\nu_0$. In comparison, in MSCPT, the darkness of the low-n states is further protected by CPT, and $T5$ is almost constant, indicating its robustness as a cooling method.

However, when R is much smaller than ν_0, RSC produces a lower $T5$ than MSCPT. Here the narrow Raman width causes a steplike change in $\mathcal{B}(n)$ across $n = \Delta n$ in RSC, whereas in MSCPT, the finite width of the CPT resonance tends to blur the contrast. In practice, as Fig. 7(b) shows, τ_2 for both RSC and MSCPT sharply increases as R becomes smaller. Although not shown in the figure, at $R = \nu_0/10$, τ_2 reaches 0.75 and 3 s for RSC and MSCP, respectively, making it impractical to excessively reduce R. In the opposite limit of a large R, the time constants of RSC become vanishingly small, whereas those of MSCPT do not significantly change because the cooling dynamics is limited by the diffusive process of population trapping. The decoherence rate γ_{12} is one of the most critical parameters in the MSCPT scheme. The $T5/T_R$ of MSCPT versus $\log_{10}(\gamma_{12}/\gamma_{12}^0)$, with $\gamma_{12}^0 = 2\pi \times 1$ Hz, are shown as a blue solid curve with circles in Fig. 8(a). The red dashed line represents $T5/T_R$ of RSC. When the temperature is below T_R, $T5$ based on $P5$ is no longer a sensitive measure of temperature, and in Fig. 8(a) we include $T0$ defined from the ground-state population $P(0)$ using $T0 = -\hbar\nu_0/k_B \ln[1 - P(0)]$ as a green dashed curve with circles. The discrepancy between $T5$ and $T0$ is a signature of the deviation from the MB distribution. In the limit of a small γ_{12}, the CPT phenomenon becomes prominent and the atoms accumulate

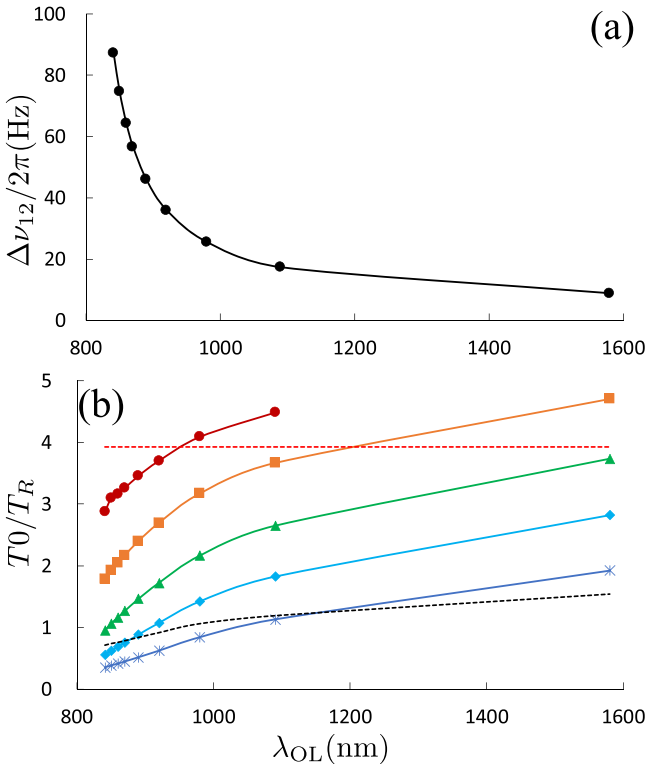

FIG. 9. (a) Plot of $\Delta\nu_{12}$ versus the lattice wavelength λ_{OL} when $w_0 = 10$ μm and the well depth in units of k_B is 125 μK. As λ_{OL} approaches the D_1 transition, both $\Delta\nu_{12}$ and γ_{12} increase as $1/\Delta_{D1}$. Here Δ_{D_1} is the detuning of λ_{OL} from the D_1 transition. (b) Plot of $T0/T_R$ of MSCPT versus λ_{OL} for a few γ_{12}. From the uppermost to the lowest curve, $\gamma_{12}/2\pi = 10$, 3, 1, 0.3, and 0.1 Hz. The red dashed line represents $T0/T_R$ of RSC. The black dashed curve denotes $T0/T_R$ of MSCPT when $\gamma_{12} = R_{OL}$ of a given λ_{OL}. The points below the black dashed curve are unattainable in our model system.

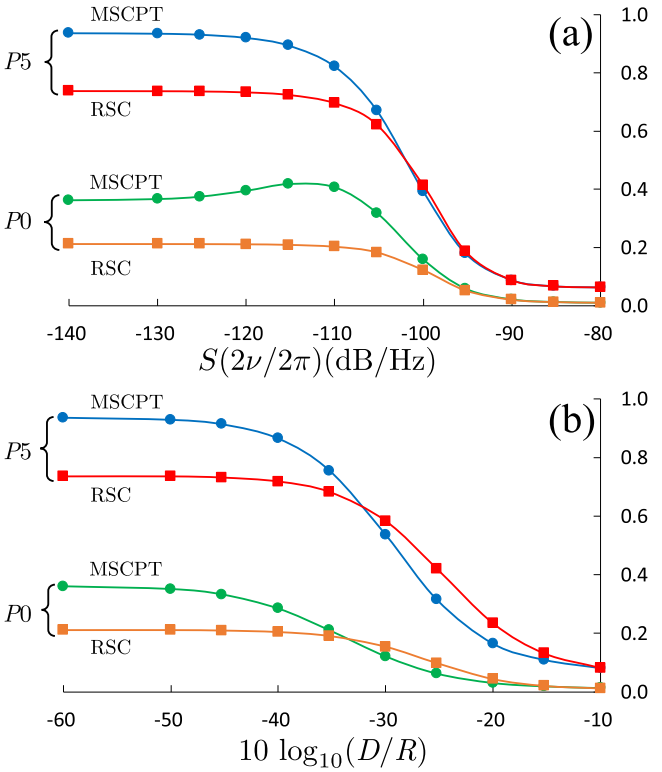

FIG. 10. (a) Plot of $P5$ of MSCPT (blue circles) and RSC (red squares) and $P0$ of MSCPT (green circles) and RSC (orange squares) versus $S(2\nu/2\pi)$, the power spectral density of the fractional intensity noise, in dB/Hz. Here $P0$ of MSCPT has a peak at $S \simeq -115$ dB/Hz. (b) Plot of $P5$ of MSCPT (blue circles) and RSC (red squares) and $P0$ of MSCPT (green circles) and RSC (orange squares) versus $10\log_{10}(D/R)$. Here D is the effective decay rate of the target states $|\phi_1\rangle$ and $|\phi_2\rangle$, due to their unintended transition by the optical pumping beam, and the decay rate R of the $|\phi_3\rangle$ state is equal to ν_0.

in the $n = 0$ state. When $\gamma_{12} = \gamma_{12}^0/10$, $T0$ is as low as T_R. This implies that, using MSCPT, subrecoil cooling is possible even when $\eta_{LD} = 1$. However, reducing γ_{12} to $\gamma_{12}^0/10$ is challenging. In our previous work on ^{7}Li using rf fields [7], we achieved $\gamma_{12}^0/4$, limited by the magnetic-field noise. The final limit on γ_{12} for an atom in an optical lattice originates from the scattering rate R_{OL} of the lattice photons [17]. In our model system of $\lambda_{OL} = 980$ nm, $w_0 = 10$ μm, and well depth of 125 μK, $R_{OL} = \gamma_{12}^0/6$. Another difficulty associated with a small γ_{12} is the increase in τ_2 of $T5$, as shown in Fig. 8(b). It is difficult to calculate τ_2 of $T0$ at a small γ_{12} owing to the slow convergence and we only estimate that it is a few times larger than τ_2 of $T5$. At the other limit of γ_{12} larger than $30\gamma_{12}^0$, Fig. 8(a) shows that MSCPT produces higher $T5$ than RSC. The mechanism for this is unclear and we suspect that the large γ_{12} broadens the CPT width, reducing the contrast in the darkness. Considering these results, the experimentally interesting range is 0.1 Hz $\leqslant \gamma_{12}/2\pi \leqslant 10$ Hz, which is shaded in Fig. 8(a). We can also improve the motional selectivity by increasing $\Delta\nu_{12}$. When λ_{OL} approaches 795 nm of the D_1 transition, the ratio β/α and thereby $\Delta\nu_{12}$ at a fixed well depth increases as $1/\Delta_{D_1}$. Here Δ_{D_1} is the detuning of the lattice beam from the D_1 transition. Figure 9(a) shows $\Delta\nu_{12}$ versus λ_{OL} when $w_0 = 10$ μm and the well depth in units of k_B is 125 μK so that $\eta_{LD} = 1$. At $\lambda_{OL} = 841$ nm, $\Delta\nu_{12}$ is as large as $2\pi \times 87$ Hz, facilitating the selection of the $n = 0$ state by CPT. However, as λ_{OL} approaches the D_1 transition, the scattering rate R_{OL} at a fixed well depth and consequently γ_{12} also increases as $1/\Delta_{D_1}$, offsetting the advantage. Figure 9(b) shows $T0/T_R$ of MSCPT versus λ_{OL} for a few $\gamma_{12}/2\pi$ from 10 Hz of the uppermost curve to 0.1 Hz of the lowest one. The red dashed line represents $T0/T_R$ of RSC and the black dashed curve shows $T0/T_R$ of MSCPT when $\gamma_{12} = R_{OL}$ for a given λ_{OL}. The points below the black dashed curve are unattainable experimentally in our model system.

Finally, we consider the effects of parametric heating and an imperfect optical pumping. They are respectively parametrized by the transition rate $Q_{\pm}(n)$ from $|\chi(n)\rangle$ to $|\chi(n \pm 2)\rangle$ in Eq. (11) and the effective decay rate D of the $|\phi_1\rangle$ and $|\phi_2\rangle$ states. In Fig. 10(a), $P5$ and $P0$ of MSCPT and RSC versus the power spectral density of the fractional intensity noise $S(2\nu/2\pi)$ in dB/Hz are plotted. The $P5$ of MSCPT and RSC suffers similarly from the parametric heating and its effect becomes insignificant when S is below -125 dB/Hz. Noise can be lowered to this level by appropriate power stabilization [18]. The $P0$ of MSCPT presents a peak

at $S \simeq -115$ dB/Hz. The incoherent transition driven by the power noise contributes an additional dephasing rate $Q(n)$ to γ_{12} of $\dot{\eta}_{12}(n,n)$ as expressed in Eq. (12b). Because $Q_{\pm}(n)$ is approximately proportional to n^2, the relative darkness of the $n=0$ state is increased. This is similar to cooling by selective parametric excitation and subsequent ejection of high-n states in an anharmonic optical trap [19]. In Fig. 10(b), $P5$ and $P0$ of MSCPT and RSC versus $10\log_{10}(D/R)$ are plotted, where the optical pumping rate R is equal to ν_0. When the rate D of the unintended transition out of the target states is five orders of magnitude smaller than the intended rate R, the effect of the imperfect optical pumping is negligible. The rate D may originate from an incorrect retardation $\delta\Gamma$ of a waveplate or misalignment $\delta\theta$ between the quantization axis and the pumping beam direction. Here D/R is typically on the order $\delta\Gamma^2$ or $\delta\theta^2$, and these errors need to be kept below a few times 10^{-3} rad. The effect of D on MSCPT is more severe than that on RSC because D also degrades the coherence of a CPT state. However, while the RSC scheme on an alkali-metal atom always requires repumping, the inverted Y configuration of MSCPT does not need it, and the target states $|\phi_1\rangle$ and $|\phi_2\rangle$ are 6.8 GHz detuned from the optical pumping transition. We expect that, in practice, D can be maintained much smaller in MSCPT.

V. DISCUSSION AND OUTLOOK

Although we used a 1D model for the numerical simulations, the configuration of Raman beams for MSCPT in the inset of Fig. 2 allows momentum transfer $\hbar\Delta\vec{k}_p = \hbar\Delta\vec{k}_q$ in the xy plane. If the confining potential of an optical trap is isotropic in the xy plane, the configuration provides cooling along the $(\hat{x}+\hat{y})/\sqrt{2}$ axis only and the motion along the $(\hat{x}-\hat{y})/\sqrt{2}$ axis is cooled only diffusively. In practice, we expect intended and unintended anisotropies as well as anharmonic coupling between x and y in a trapping potential will allow 2D cooling by the configuration. In addition, for cooling along the z axis, we may apply another Raman beam $\vec{E}_z = \mathcal{E}_z\hat{x}\cos(k_z z - \omega_z t)$ so that $(\vec{E}_z, \vec{E}_p)$ and $(\vec{E}_z, \vec{E}_q)$ drive the p and q transitions, respectively. Here, by adjusting ω_z, the transitions are tuned to the red sideband of the z motion. Apparently, the resulting double Λ configuration increases the complexity of the scheme. However, in our model system of a 1D lattice, for example, the vibration frequencies along the z axis and the x and y axes differ by a factor of 50, and once an atom falls to the $n_z = 0$ state, it decouples from $\vec{E}_z$ because the Raman transitions are detuned by $50\nu_0$, while their widths are order ν_0. Here n_z is the motional quantum number along z.

The configuration in Fig. 1(a) is closed, and any of the three $5S_{1/2}$ states can play the role of the apex state $|\phi_3\rangle$ in Fig. 1(b). One interesting possibility is to exchange the roles of the $|F=1, m_F=-1\rangle$ and $|F=2, m_F=-1\rangle$ states in Fig. 1(a) so that the latter becomes $|\phi_3\rangle$ in Fig. 1(b). In this configuration, $\Delta\nu_{12} = (3\alpha/4\beta)\nu_0$ is three times larger than the original $\Delta\nu_{12}$ in Eq. (3), enhancing the motional selectivity. However, whether this enhancement would lead to lower temperature is not clear because γ_{12} from magnetic-field noise is proportional to $\Delta\nu_{12}^2$. The γ_{12} in this configuration is nine times larger, and unless noise of the field-generating current is tightly controlled, the gain in $\Delta\nu_{12}$ may be lost.

In summary, we proposed a cooling scheme that combines the ideas of velocity-selective coherent population trapping and Raman sideband cooling. Using the master equations for 1D RSC and 1D MSCPT, we calculated the steady-state distribution over n and the time constants toward it when the Lamb-Dicke parameter was 1, as we changed the experimental parameters such as (i) the order of the sideband and the CPT detuning, (ii) the optical pumping rate and the Rabi frequencies of the Raman transitions, (iii) the wavelength and hence the vector polarizability of an Rb atom and the decoherence rate, and (iv) the parametric heating rate and the depumping rate. For most ranges of these parameters, MSCPT produced colder atoms than RSC, even though the recoil heating in RSC was reduced by $\frac{1}{3}$ by adjusting the branching ratio. Under a favorable condition, the temperature estimated from the $n=0$ population reached the recoil temperature $\mathcal{E}_R/k_B$ or below, indicating subrecoil cooling even outside the Lamb-Dicke regime. This improvement in cooling was quantitatively explained in terms of the reduction in the brightness of the low-n states by the CPT phenomenon.

However, this improvement has consequences. First, the MSCPT scheme is not suitable for a high-density atomic sample. The optical pumping beam, which is near resonance and stays on throughout the cooling process, mediates photoassociation and atomic collisions destroy the coherence. The MSCPT scheme is best for a single atom in a lattice site or an optical tweezer. Other problems are the slow cooling process and technical burdens to implement complex cooling beams and to control the phase noise from various sources. Under these challenges, a proof-of-principle experiment was successfully carried out in our laboratory to demonstrate the feasibility and effectiveness of the idea [9]. In the longer term, the MSCPT scheme could be applied to cool a diatomic polar molecule in an optical trap. Using a MgF molecule as an example, $\Delta\nu_{12}$ of the $|\phi_1\rangle = |F=2, m_F=-2\rangle$ and $|\phi_2\rangle = |F=2, m_F=-1\rangle$ states is 12% of the average of ν_1 and ν_2 when the trap wavelength is 532 nm. The values are when the molecule is in the electronic and vibrational ground states and the first excited rotational state and its total electronic angular momentum is $\frac{3}{2}$ and the nuclear spin is $\frac{1}{2}$. The $X\,^2\Sigma_{1/2}{}^+ \rightarrow A^2\,\Pi_{1/2}$ transition of MgF is at 359 nm. In comparison, for ^{87}Rb, $\Delta\nu_{12}/\nu_0$ is 0.7% at the benchmark $\lambda_{\mathrm{OL}} = 980$ nm and 2.5% at 841 nm. However, it is still unclear whether the complicated level structure of the molecule will allow an appropriate configuration for the MSCPT scheme. One or two repumping beams will be necessary and the recoil heating will increase. Simple simulation of the situation by decreasing the branching ratios p_1 and p_2 in our model system of Rb shows that the lowest temperature obtained by both MSCPT and RSC increases, but the advantage of MSCPT is maintained.

ACKNOWLEDGMENTS

This work was supported by the National Research Foundation of Korea (Grant No. 2019M3E4A1080382). We thank Q-Han Park for help with the numerical work, D. G. Lee for assisting in the computer setup, and Eunmi Chae for discussions and information on molecules.

APPENDIX A: MASTER EQUATIONS FOR 1D MOTION-SELECTIVE COHERENT POPULATION TRAPPING

For the Hamiltonian $H_{\mathrm{MSCPT}} = H_0 + W_p + W_q + V$, where H_0 is the sum of Eqs. (8a) and (14), W_p and W_q are given in Eqs. (8b) and (15), respectively, and V represents the radiative decay at R, the master equations are

$$\dot{\eta}_{11}(n_1, n_1') = i\frac{\Omega_p^0}{2}\sum_{n_3''}\{\eta_{13}(n_1, n_3'')\mathcal{F}_{31}(n_3'', n_1') - \mathcal{F}_{13}^*(n_1, n_3'')\eta_{31}(n_3'', n_1')\} + i(n_1' - n_1)\nu_1\eta_{11}(n_1, n_1') + \delta_{n_1,n_1'}p_1 R\sum_{n_3''}|\mathcal{F}_{13}(n_1, n_3'')|^2\eta_{33}(n_3'', n_3''), \tag{A1a}$$

$$\dot{\eta}_{22}(n_2, n_2') = i\frac{\Omega_q^0}{2}\sum_{n_3''}\{\eta_{23}(n_2, n_3'')\mathcal{F}_{32}(n_3'', n_2') - \mathcal{F}_{23}^*(n_2, n_3'')\eta_{32}(n_3'', n_2')\} + i(n_2' - n_2)\nu_2\eta_{22}(n_2, n_2') + \delta_{n_2,n_2'}p_2 R\sum_{n_3''}|\mathcal{F}_{23}(n_2, n_3'')|^2\eta_{33}(n_3'', n_3''), \tag{A1b}$$

$$\dot{\eta}_{33}(n_3, n_3') = i\frac{\Omega_p^0}{2}\sum_{n_1''}\{\eta_{31}(n_3, n_1'')\mathcal{F}_{13}^*(n_1'', n_3') - \mathcal{F}_{31}(n_3, n_1'')\eta_{13}(n_1'', n_3')\} + i\frac{\Omega_q^0}{2}\sum_{n_2''}\{\eta_{32}(n_3, n_2'')\mathcal{F}_{23}^*(n_2'', n_3') - \mathcal{F}_{32}(n_3, n_2'')\eta_{23}(n_2'', n_3')\} + \{i(n_3' - n_3)\nu_3 - R\}\eta_{33}(n_3, n_3') + \delta_{n_3,n_3'}p_3 R\sum_{n_3''}|\mathcal{F}_{33}(n_3, n_3'')|^2\eta_{33}(n_3'', n_3''), \tag{A1c}$$

$$\dot{\eta}_{13}(n_1, n_3) = i\frac{\Omega_p^0}{2}\left\{\sum_{n_1''}\eta_{11}(n_1, n_1'')\mathcal{F}_{13}^*(n_1'', n_3) - \sum_{n_3''}\mathcal{F}_{13}^*(n_1, n_3'')\eta_{33}(n_3'', n_3)\right\} + i\frac{\Omega_q^0}{2}\sum_{n_2''}\eta_{12}(n_1, n_2'')\mathcal{F}_{23}^*(n_2'', n_3) + \left[i\{(n_3 + \Delta n)\nu_3 - n_1\nu_1\} - \frac{R}{2}\right]\eta_{13}(n_1, n_3), \tag{A1d}$$

$$\dot{\eta}_{23}(n_2, n_3) = i\frac{\Omega_q^0}{2}\left\{\sum_{n_2''}\eta_{22}(n_2, n_2'')\mathcal{F}_{23}^*(n_2'', n_3) - \sum_{n_3''}\mathcal{F}_{23}^*(n_2, n_3'')\eta_{33}(n_3'', n_3)\right\} + i\frac{\Omega_p^0}{2}\sum_{n_1''}\eta_{21}(n_2, n_1'')\mathcal{F}_{13}^*(n_1'', n_3) + \left[i\{(n_3 + \Delta n)\nu_3 - n_2\nu_2 + \delta_{\mathrm{CPT}}\} - \frac{R}{2}\right]\eta_{23}(n_2, n_3), \tag{A1e}$$

$$\dot{\eta}_{12}(n_1, n_2) = \frac{i}{2}\sum_{n_3''}\{\Omega_q^0\eta_{13}(n_1, n_3'')\mathcal{F}_{32}(n_3'', n_2) - \Omega_p^0\mathcal{F}_{13}^*(n_1, n_3'')\eta_{32}(n_3'', n_2)\} + \{i(n_2\nu_2 - n_1\nu_1 - \delta_{\mathrm{CPT}}) - \gamma_{12}\}\eta_{12}(n_1, n_2), \tag{A1f}$$

$\dot{\eta}_{31}(n_3, n_1) = \dot{\eta}_{13}^*(n_1, n_3)$, $\dot{\eta}_{32}(n_3, n_2) = \dot{\eta}_{23}^*(n_2, n_3)$, and $\dot{\eta}_{21}(n_2, n_1) = \dot{\eta}_{12}^*(n_1, n_2)$.

APPENDIX B: RECURSION RELATIONS FOR $\mathcal{F}(n, l)$

The $\mathcal{F}$ factor in one dimension is defined as

$$\mathcal{F}_{ij}(n_i, n_j) = \langle\chi_i(n_i)|e^{ik_p x}|\chi_j(n_j)\rangle. \tag{B1}$$

As a specific example, we consider $\mathcal{F}_{31}(n_3, n_1)$; set $n_3 = n$, $n_1 = l$, and $k_p = k$; and omit the subscript 31 from $\mathcal{F}$ for simplicity. Explicitly,

$$\mathcal{F}(n, l) = C_n(a_3)C_l(a_1)\int_{-\infty}^{+\infty}H_n(a_3 x)H_l(a_1 x)e^{-\langle a^2\rangle x^2 + ikx}dx, \tag{B2}$$

where $a_1 = \sqrt{\nu_1 m/\hbar}$ and $C_l(a_1) = \sqrt{a_1/\pi^{1/2}2^l l!}$, with m the atomic mass. The a_3 and $C_n(a_3)$ are similarly defined and $\langle a^2\rangle = (a_1^2 + a_3^2)/2$. Integrating by parts and using the recursion relations of the Hermite polynomials, we obtain the recursion relation

for $\mathcal{F}(n,l)$,

$$\mathcal{F}(n,l) = i\frac{ka_1}{\langle a^2\rangle}\sqrt{\frac{1}{2n}}\mathcal{F}(n-1,l) + \frac{\Delta a^2}{2\langle a^2\rangle}\sqrt{\frac{n-1}{n}}\mathcal{F}(n-2,l) + \frac{a_1a_3}{\langle a^2\rangle}\sqrt{\frac{l}{n}}\mathcal{F}(n-1,l-1), \tag{B3}$$

where $\Delta a^2 = a_3^2 - a_1^2$. Alternatively,

$$\mathcal{F}(n,l) = i\frac{ka_3}{\langle a^2\rangle}\sqrt{\frac{1}{2l}}\mathcal{F}(n,l-1) - \frac{\Delta a^2}{2\langle a^2\rangle}\sqrt{\frac{l-1}{l}}\mathcal{F}(n,l-2) + \frac{a_1a_3}{\langle a^2\rangle}\sqrt{\frac{n}{l}}\mathcal{F}(n-1,l-1). \tag{B4}$$

When $\nu_1 = \nu_3$, $\Delta a^2 = 0$ and the relation is simplified.

To obtain $\mathcal{F}$ factor for a transition driven by a radio-frequency field, we substitute $k = 0$ in Eq. (B2). When $\nu_1 = \nu_3$, $\mathcal{F}(n,l) = \delta_{nl}$. When $\nu_1 \neq \nu_3$, the recursion relations cannot be obtained by simply substituting $k = 0$ in Eqs. (B3) and (B4) and a separate calculation yields

$$\begin{aligned}\mathcal{F}(n,l) = &\sqrt{\frac{(n-1)(l-1)}{nl}}\mathcal{F}(n-2,l-2) + \frac{a_1a_3}{\langle a^2\rangle}\sqrt{\frac{1}{nl}}\mathcal{F}(n-1,l-1) \\ &+ \frac{\Delta a^2}{2\langle a^2\rangle}\sqrt{\frac{n-1}{n}}\mathcal{F}(n-2,l) - \frac{\Delta a^2}{2\langle a^2\rangle}\sqrt{\frac{l-1}{l}}\mathcal{F}(n,l-2).\end{aligned} \tag{B5}$$

In our previous publication on rf spectroscopy [16], we used a series expansion of $H_n(a_i x)$ in terms of $(a_i - \bar{a})/\bar{a}$ with $\bar{a} = \sqrt{\langle a^2\rangle}$ for $i = 1, 3$ to speed up the evaluation of $\mathcal{F}(n,l)$. The recursion relation (B5) is much more efficient.

[1] F. Diedrich, J. C. Bergquist, W. M. Itano, and D. J. Wineland, Laser Cooling to the Zero-Point Energy of Motion, Phys. Rev. Lett. **62**, 403 (1989).

[2] A. Aspect, E. Arimondo, R. Kaiser, N. Vansteenkiste, and C. Cohen-Tannoudji, Laser Cooling below the One-Photon Recoil Energy by Velocity-Selective Coherent Population Trapping, Phys. Rev. Lett. **61**, 826 (1988).

[3] S. E. Hamann, D. L. Haycock, G. Klose, P. H. Pax, I. H. Deutsch, and P. S. Jessen, Resolved- Sideband Raman Cooling to the Ground State of an Optical Lattice, Phys. Rev. Lett. **80**, 4149 (1998).

[4] V. Vuletić, C. Chin, A. J. Kerman, and S. Chu, Degenerate Raman Sideband Cooling of Trapped Cesium Atoms at Very High Atomic Densities, Phys. Rev. Lett. **81**, 5768 (1998).

[5] G. Grynberg and J.-Y. Courtois, Proposal for a magneto-optical lattice for trapping atoms in nearly-dark states, Europhys. Lett. **27**, 41 (1994).

[6] F. Bardou, J. P. Bouchaud, O. Emile, A. Aspect, and C. Cohen-Tannoudji, Subrecoil Laser Cooling and Lévy Flights, Phys. Rev. Lett. **72**, 203 (1994).

[7] H. Kim, H. S. Han, T. H. Yoon, and D. Cho, Coherent population trapping in a Λ configuration coupled by magnetic dipole interactions, Phys. Rev. A **89**, 032507 (2014).

[8] Y. Sagi, I. Almog, and N. Davidson, Universal Scaling of Collisional Spectral Narrowing in an Ensemble of Cold Atoms, Phys. Rev. Lett. **105**, 093001 (2010).

[9] S. Park, M. H. Seo, R. A. Kim, and D. Cho, Motion-selective coherent population trapping by Raman sideband cooling along two paths in a Λ configuration, preceding paper, Phys. Rev. A **106**, 023323 (2022).

[10] L. Anderegg, B. L. Augenbraun, Y. Bao, S. Burchesky, L. W. Cheuk, W. Ketterle, and J. M. Doyle, Laser cooling of optically trapped molecules, Nat. Phys. **14**, 890 (2018).

[11] J. Qi, Electromagnetically induced transparency in an inverted Y-type four-level system, Phys. Scr. **81**, 015402 (2010).

[12] D. Cho, Analogous Zeeman effect from the tensor polarizability in alkali atoms, J. Korean Phys. Soc. **30**, 373 (1997).

[13] C. Cohen-Tannoudji, J. Dupont-Roc, and G. Grynberg, *Atom-Photon Interactions: Basic Processes and Applications* (Wiley, New York, 1992), pp. 518–524.

[14] T. A. Savard, K. M. O'Hara, and J. E. Thomas, Laser-noise-induced heating in far-off resonance optical traps, Phys. Rev. A **56**, R1095 (1997).

[15] The processor is the 11th Gen Intel(R) Core(TM) i9-11900K @ 3.50GHz with 128 kB of memory.

[16] S. Park, M. H. Seo, and D. Cho, Ground-state hyperfine spectroscopy of ^{87}Rb atoms in a 1D optical lattice, J. Phys. B **52**, 235002 (2019).

[17] H. Uys, M. J. Biercuk, A. P. VanDevender, C. Ospelkaus, D. Meiser, R. Ozeri, and J. J. Bollinger, Decoherence due to Elastic Rayleigh Scattering, Phys. Rev. Lett. **105**, 200401 (2010).

[18] F. Tricot, D. H. Phung, M. Lours, S. Guérandel, and E. de Clercq, Power stabilization of a diode laser with an acousto-optic modulator, Rev. Sci. Instrum. **89**, 113112 (2018).

[19] N. Poli, R. J. Brecha, G. Roati, and G. Modugno, Cooling atoms in an optical trap by selective parametric excitation, Phys. Rev. A **65**, 021401(R) (2002).